applied sciences

MDPI

Article

Influence of Gap Width on Temporal Nonlinear Behaviors in CO_2 Dielectric Barrier Discharges under Martian Conditions

Xucheng Wang, Shuhan Gao and Yuantao Zhang *

School of Electrical Engineering, Shandong University, Jinan 250061, China
* Correspondence: ytzhang@sdu.edu.cn

Abstract: In recent years, the in situ resource utilization of CO_2 on Mars for oxygen and carbon monoxide production has attracted increasing attention. Dielectric barrier discharges (DBDs) have great potential for large-scale industrial application of CO_2 decomposition, and the nonlinear behaviors of DBDs are directly related to the discharge stability. In this paper, a fluid model is built to investigate the influence of gap width on temporal nonlinear behaviors in CO_2 DBDs driven by tailored voltages under Martian conditions (the pressure and temperature are 4.5 Torr and 210 K, respectively). The simulation results show that, with the increase in the gap width, the discharge evolves from period-one state into period-two state, then changes into chaos, and finally undergoes an inverse period-doubling bifurcation from reverse period-two discharge to period-one discharge. After the CO_2 discharge is extinguished, the electron density drops rapidly, and the dominant charged particles in the discharge region are heavy CO_3^- and CO_2^+ ions. As the gap width increases, the heavy ions produced by the previous discharge cannot be completely dissipated and stay in the sheath region, which makes the subsequent discharge easy to be ignited and reduces the breakdown voltage, leading to the evolution from period-one discharge to period-two discharge. When the gap width is increased to 5 mm, a lot of charged particles stay in the discharge gap, and these charged particles, especially electrons, are driven to the electrodes by the applied voltage, forming a reverse electric field, which inhibits the development of positive discharge and facilitates the formation of negative discharge. Then, as the gap width continues to increase, the density and spatial distribution of residual ions in the sheath region at the beginning of the negative discharge for two consecutive voltage periods are gradually equal, resulting in the discharge evolution from reverse period-two state to reverse period-one state. This study could deepen the understanding of the underpinning physics of nonlinear behaviors, and provide a groundwork for actively regulating the evolution of nonlinear behaviors.

Keywords: electrode gap; nonlinear behavior; CO_2 discharges; Martian pressure

check for updates

Citation: Wang, X.; Gao, S.; Zhang, Y. Influence of Gap Width on Temporal Nonlinear Behaviors in CO_2 Dielectric Barrier Discharges under Martian Conditions. *Appl. Sci.* **2022**, *12*, 10990. https://doi.org/10.3390/app122110990

Academic Editor: Emilio Martines

Received: 21 September 2022
Accepted: 24 October 2022
Published: 30 October 2022

Publisher's Note: MDPI stays neutral with regard to jurisdictional claims in published maps and institutional affiliations.

Copyright: © 2022 by the authors. Licensee MDPI, Basel, Switzerland. This article is an open access article distributed under the terms and conditions of the Creative Commons Attribution (CC BY) license (https://creativecommons.org/licenses/by/4.0/).

1. Introduction

With the increasingly rapid advances of Mars exploration, how to convert Mars resources into propellants and life support consumables has attracted great attention [1,2]. As the most abundant component in the Martian atmosphere [3], CO_2 can be used as a feedstock for In Situ Resource Utilization (ISRU) to produce CO and O_2 [4]. The O_2 could provide materials for life support and improve the Martian atmosphere, and CO has been proposed for the production of spacecraft propellants [5,6]. The ISRU can reduce the launch mass of space vehicles and lower the risk of crew and space missions. However, due to the high stability of CO_2 molecules, substantial thermal energy input is required in the decomposition of CO_2, which is a great challenge for ISRU of CO_2 on Mars. It is possible to convert CO_2 into chemicals and fuels using traditional approaches such as thermal catalysis, but the main issues are high energy consumption and low productivity [7]. In fact, non-thermal plasma is an effective technology for molecular activation, the energetic electrons produced in the non-thermal plasma are capable of breaking the double bonds (O=C=O) in

CO_2 molecules at a low temperature without heating the entire gas, effectively reducing the energy consumption [8]. In addition, the Martian environment has many advantages for the local decomposition of CO_2 using non-thermal plasma. On the one hand, the average atmospheric pressure on Mars is only 4.5 Torr, which is considered to be close to the ideal for plasma reforming and can make CO_2 gas easy to be ignited at a lower voltage [9–11]. On the other hand, the low temperature of the Martian atmosphere with an average value of about 210 K can limit the gas heating effect and enhance vibrational up-pumping along the asymmetric stretching mode, which is considered the most efficient approach for the decomposition of CO_2 [12,13]. In addition, the cold surrounding atmosphere can also slow down the reaction of the recombination of CO and O to generate CO_2 [11]. In addition, a small amount of N_2 (about 2.7%) and Ar (about 1.6%) in the Martian atmosphere facilitate the decomposition of CO_2 molecules. N_2 could transfer vibrational energy to CO_2 molecules, which pumps CO_2 molecules into asymmetric stretching modes [14], Ar could slightly improve the electron energy distribution function (EEDF), enhancing the electron impact processes [15]. Furthermore, the extreme flexibility and immediate switch of non-thermal plasma enable the harvesting of energy from solar power [16,17].

At present, a large number of studies have discussed the decomposition of CO_2 under atmospheric pressure by using plasma technology [18–24], which lays the groundwork for investigating CO_2 conversion under Martian conditions. Due to the widespread applications in the industrial fields, dielectric barrier discharge (DBD) has attracted wide-ranging interest in CO_2 conversion and has become one of the most potential candidates for ISRU [25–27]. However, as a typical nonlinear dynamical system, DBD can possess abundant temporal nonlinear behaviors such as asymmetric discharge, quasiperiodicity, period-doubling bifurcation, and chaos [28–31]. Through the experimental measurements, Dai et al. [32] reported that, by increasing the amplitude of voltage, the discharge in atmospheric helium can undergo an inverse period-doubling bifurcation from chaotic state to period-one state. Shi et al. [33] investigated the temporal nonlinear behaviors in argon atmospheric DBDs based on a fluid model, and found that, by increasing the driving frequency, the discharge can enter chaotic discharge via a period-doubling bifurcation and then return stable periodic discharge via an inverse period-doubling bifurcation. The simulation results of Li et al. [34] showed that the chaotic state in atmospheric helium DBDs could change into an asymmetric period-one state by adding nitrogen to helium. The disturbance of residual positive column is considered to be the main reason for the formation of asymmetric discharge [35,36]. However, some recent reports pointed out that the reason for the transition between asymmetric discharge and symmetric discharge is the electron backflow effect [37].

It is clear that most studies up to now on nonlinear behaviors in DBD have mainly focused on the formation mechanism of asymmetric discharges with the working gas of helium and argon, although the periodic discharges have been obtained in experiments and simulations, and the formation mechanism of periodic discharges has not been closely examined. In addition, as an electronegative gas, the discharge characteristic of CO_2 are significantly different from that of inert gases. After the discharge is extinguished, the electron density could decrease rapidly, and the main charged particles in the discharge gap are the heavy ions of CO_2^+ and CO_3^- [23,38]. Furthermore, the temporal nonlinear behaviors are directly associated with the stability of CO_2 discharge, and a deeper insight into the formation mechanism of nonlinear behaviors in CO_2 DBDs under Martian conditions is beneficial to obtaining stable discharges on Mars.

Changing the gap width could regulate the transport of charged particles, resulting in the appearance of nonlinear behaviors. Thus, in the present study, based on a 1D fluid model, the underpinning physics of temporal nonlinear behaviors in CO_2 DBD under Martian conditions is investigated by varying the gap width. The remaining part of this paper is as follows: Section 2 is concerned with the brief description of the mathematical model and reaction set used in this paper. In Section 3, based on the numerical data, the evolution and formation mechanisms of nonlinear behaviors in CO_2 discharges are

carefully discussed when the gap width is increased. Finally, a conclusion is summarized in Section 4.

2. Description of the Model

A fluid model is applied in this paper to investigate the effect of the gap width on temporal nonlinear behaviors in CO_2 DBDs under Martian conditions. In this model, the continuity equations coupled with the drift–diffusion approximation describe the dynamic behaviors of each neutral and charged species, the Poisson equation is used to obtain the electric field in the discharge region, and the electron energy balance equation is also incorporated to calculate the electron temperature [39–41].

$$\frac{\partial N_{\mathrm{e,a,i,n}}}{\partial t} + \frac{\partial \Gamma_{\mathrm{e,a,i,n}}}{\partial x} = R_{\mathrm{e,a,i,n}} \tag{1}$$

$$\Gamma_{\mathrm{e,a,i,n}} = \mp \mu_{\mathrm{e,a,i}} N_{\mathrm{e,a,i}} E - D_{\mathrm{e,a,i,n}} \frac{\partial N_{\mathrm{e,a,i,n}}}{\partial x} \tag{2}$$

$$\varepsilon_0 \frac{\partial E}{\partial x} = e_0 \left(\sum_i N_i - \sum_a N_{\mathrm{e},a} \right) \tag{3}$$

$$\frac{\partial}{\partial t}\left(\frac{3}{2} k_{\mathrm{b}} N_{\mathrm{e}} T_{\mathrm{e}}\right) = -\frac{\partial Q_{\mathrm{e}}}{\partial x} - e_0 \Gamma_{\mathrm{e}} E - \sum_j k_j N_{\mathrm{e}} N_j H_j - 3 k_{\mathrm{b}} N_{\mathrm{e}} \frac{m_{\mathrm{e}}}{m_{\mathrm{g}}} \left(T_{\mathrm{e}} - T_{\mathrm{g}}\right) \overline{\nu_{\mathrm{e}}} \tag{4}$$

where the indices e, a, i, and n are electrons, negative ions, positive ions, and neutral particles, respectively. N and Γ are the density and flux of species, respectively. R is the source and lose items of species. μ and D are the mobility and diffusion coefficients, respectively, and only the diffusion item is considered for neutral particles. ε_0 is the vacuum permittivity and e_0 is the elementary charge. E denotes the electric field in the discharge region. k_b is the Boltzmann constant. Q_{e} is the electron thermal flux. k_j and H_j are the reaction rate and threshold energy of the inelastic impact reaction j, respectively. m_{e}, m_{g}, T_{e}, and T_{g} are the electron mass, gas species mass, electron temperature, and gas temperature, respectively. $\overline{\nu_e}$ denotes the electron momentum transfer collision frequency with the background gas, which is obtained from Ref. [42].

The total current density $I_0(t)$ is given as

$$I_0 = \frac{\varepsilon_0}{d_{\mathrm{g}} + 2d_{\mathrm{s}}/\varepsilon_{\mathrm{r}}} \frac{\mathrm{d}V_{\mathrm{a}}}{\mathrm{d}t} + \frac{1}{d_{\mathrm{g}} + 2d_{\mathrm{s}}/\varepsilon_{\mathrm{r}}} \int_0^{d_{\mathrm{g}}} j_{\mathrm{g}} \mathrm{d}x \tag{5}$$

where d_{g} denotes the gap width. d_{s} and ε_{r} represent the the thickness and relative permittivity of the dielectric barriers, respectively. j_{g} is the conduction current density, which is determined by $j_{\mathrm{g}} = e_0 \left(\sum_i \Gamma_i - \sum_a \Gamma_{\mathrm{e},a} \right)$.

In this paper, the applied voltage V_{a} with the power-on phase (P_{on}) and power-off phase (P_{off}) is described by a segmented function, which is given by

$$V_{\mathrm{a}} = \begin{cases} V_0 \sin(2\pi f t) & t \in P_{\mathrm{on}} \\ 0 & t \in P_{\mathrm{off}} \end{cases} \tag{6}$$

where V_0 is the amplitude of the sinusoidal voltage, and f is the driving frequency. The waveform of applied voltage is given in Figure 1, where a positive half-cycle sinusoidal voltage with a voltage amplitude of 1500 V and a driving frequency of 50 kHz is applied during the power-on phase, and no negative voltage is applied. In addition, the applied voltage is set to zero during the power-off phase. The durations of power-on phase and power-off phase are fixed at 10 μs.

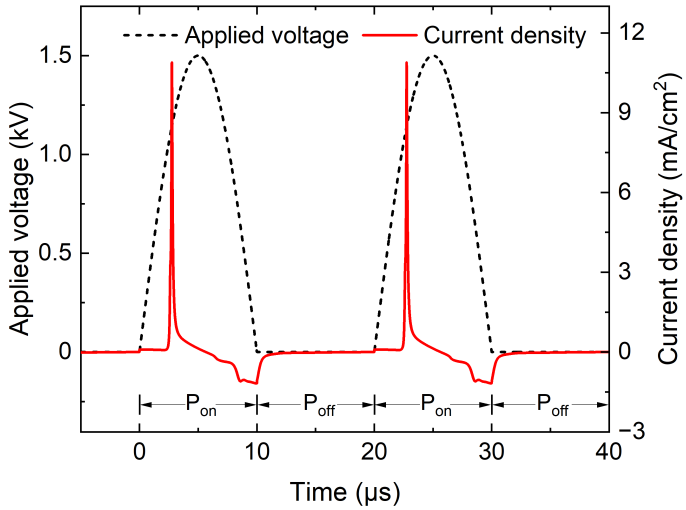

Figure 1. Waveform of applied voltage and corresponding current density in the simulation.

The derivative of gas voltage is expressed as

$$\frac{\partial V_{\mathrm{g}}}{\partial t} = \frac{d_{\mathrm{g}}}{d_{\mathrm{g}} + 2d_{\mathrm{s}}/\varepsilon_{\mathrm{r}}} \frac{\mathrm{d}V_{\mathrm{a}}}{\mathrm{d}t} - \frac{2d_{\mathrm{s}}}{\varepsilon_0 \varepsilon_{\mathrm{r}} \left(d_{\mathrm{g}} + 2d_{\mathrm{s}}/\varepsilon_{\mathrm{r}}\right)} \int_0^{d_{\mathrm{g}}} j_{\mathrm{g}} \mathrm{d}x \tag{7}$$

The memory voltage $V_{\mathrm{m}}(t)$, which is the total voltage fall across the two dielectric barriers, is given by

$$V_{\mathrm{m}} = V_{\mathrm{a}} - V_{\mathrm{g}} \tag{8}$$

In this paper, the CO_2 discharge is generated and sustained in a parallel-plate DBD structure, and each electrode is covered by a dielectric barrier with a thickness of 1.0 mm and a permittivity of 6.1. At the boundary of the discharge gap, the following surface reactions are considered in this model: excited CO_2 molecules are quenched to their ground state and ions are neutralized to their corresponding neutral species [43]. In addition, the boundary conditions for the flux of various particles and electron energy are adopted as follows [44,45]:

$$\Gamma_{\mathrm{e}} \cdot n = \frac{1}{4} N_{\mathrm{e}} \sqrt{\frac{8 k_{\mathrm{b}} T_{\mathrm{e}}}{\pi m_{\mathrm{e}}}} - \alpha N_{\mathrm{e}} \mu_{\mathrm{e}} E \cdot n - \sum_k \gamma_k (\Gamma_k \cdot n) \tag{9}$$

$$\Gamma_k \cdot n = \frac{1}{4} N_{\mathrm{e}} \sqrt{\frac{8 k_{\mathrm{b}} T_k}{\pi m_k}} + \alpha \mathrm{sgn}(q_k) q_k N_k \mu_k E \cdot n \tag{10}$$

$$n \cdot \Gamma_\varepsilon = \frac{5}{6} N_\varepsilon \sqrt{\frac{8 k_{\mathrm{b}} T_{\mathrm{e}}}{\pi m_{\mathrm{e}}}} - \alpha N_\varepsilon \mu_\varepsilon E \cdot n - \sum_k \gamma_k \varepsilon_k (\Gamma_k \cdot n) \tag{11}$$

where the indices e, k, and ε represent electrons, heavy particles, and electron energy, respectively. q_k is the charge number of the particle k, and $\mathrm{sgn}(q_k)$ is the sign of q_i, which is positive (+) for positive ions, negative (−) for electrons and negative ions, and nil for neutral particles, respectively. The secondary electron emission is considered in this model, and the emission coefficient γ_k and the initial energy ε_k of secondary electrons are 0.03 and 2.5 eV, respectively. n is the normal vector pointing to the dielectric barrier. α is a switch function depending on the product of E and n, which is defined as

$$\alpha = \begin{cases} 0 & (\mathrm{sgn}(q_k) E \cdot n \leqslant 0) \\ 1 & (\mathrm{sgn}(q_k) E \cdot n > 0) \end{cases} \tag{12}$$

To more accurately clarify the mechanism of temporal nonlinear behaviors in CO_2 DBDs under Martian conditions, based on graph theory proposed by Holmes and Mu-

rakami [46,47], the reaction set of CO_2 is selected using a 0D kinetic model. According to Ref. [38], six neutral species and seven charged species are considered. Moreover, an electronically excited state of CO_2 (i.e., CO_2e_1), four lower symmetric stretching and bending mode of CO_2 (denoted as CO_2v_a,CO_2v_b,CO_2v_c, and CO_2v_{1a}), and eight asymmetric stretching mode of CO_2 (symbolized as CO_2v_1, CO_2v_2, CO_2v_3, CO_2v_4, CO_2v_5, CO_2v_6, CO_2v_7, and CO_2v_8) are also taken into consideration. These species taken into account in the chemical model are given in Table 1. The chemical reactions and the corresponding reaction rate coefficients are obtained from the previous investigation in Ref. [38]. The reaction rate coefficient for electron impact processes and the transport coefficients for electrons are calculated using BOLSIG+ based on the cross sections obtained from the IST-Lisbon database available on the open-access LXCat website [48,49].

Table 1. Species taken into account in the chemical model.

Radicals and Molecules	Charged Species	Excited Species
CO_2, CO, C, O, O_2, O_3	e, O^-, O_2^-, CO_3^-, CO_4^-, CO_2^+, O_2^+	CO_2e_1, CO_2v_a,CO_2v_b,CO_2v_c,CO_2v_{1a} CO_2v_1, CO_2v_2, CO_2v_3, CO_2v_4 CO_2v_5, CO_2v_6, CO_2v_7, CO_2v_8

The reduced mobility μ of ions in CO_2 gas under Martian conditions is given by [50,51]

$$\mu = \mu_0 \left(\frac{760}{P}\right)\left(\frac{T_g}{273.15}\right) \tag{13}$$

where μ_0 denotes the standard mobility corresponding to the ideal gas at 760 Torr and 273.15 K. P and T_g are the average pressure and temperature of the Martian atmosphere with the values of 4.5 Torr and 210 K, respectively. The standard mobilities of ions in CO_2 gas are obtained from Refs. [51–53], and the corresponding diffusion coefficients can be deduced from the Einstein relation [48]. In addition, the reduced diffusion coefficients D of neutral species are calculated from

$$D = D_0 \left(\frac{760}{P}\right)\left(\frac{T_g}{273.15}\right)^{\beta} \tag{14}$$

where D_0 is the standard diffusion coefficient obtained from Refs. [53–56], and the value of β is determined by the neutral species [57]. Except for the background gas CO_2 molecules, the initial densities for the other neutral species are 1.0×10^5 cm^{-3}. To maintain electrical neutrality of the CO_2 plasma, the initial densities of electron, O^-, O_2^-, CO_3^-, and CO_4^- are set to be 1.0×10^5 cm^{-3}, and the initial densities of CO_2^+ and O_2^+ are set to be 2.5×10^5 cm^{-3}, respectively.

3. Results and Discussion

By increasing the gap width from 4 to 5.2 mm under the same simulation conditions, the evolution of temporal nonlinear behaviors in CO_2 discharges is numerically investigated, the DBDs are driven by a tailored sinusoidal voltage with power-on and power-off phases. As shown in Figure 1, only a large current pulse is generated during the power-on phase, and the charged particles produced by the discharge can move toward the surface of dielectric barriers during the power-off phase. In fact, according to previous work [38], when the CO_2 discharge is extinguished, electrons can quickly reach the surface of the dielectric barrier, and the dominant charged particles in the discharge region are heavy CO_2^+ and CO_3^- ions, which could slowly migrate to the electrodes. Thus, when the gap width is increased, these ions cannot reach the barriers during the power-off phase and stay in the discharge gap, which affects the electric field for the next discharge. In other words, an increase in the gap width can prolong the time for charged particles to reach the surface of barriers, affecting the density and position of the residual charged particles, which results

in the formation of nonlinear behaviors. The simulation results show that the temporal nonlinear behaviors are very sensitive to the changes in the control parameters and can be maintained over a gap width interval. To more clearly display the effects of gap width and the transformation mechanism of nonlinear behaviors, several typical nonlinear behaviors under different gap widths are selected. For example, when the gap width is increased to about 4.2 mm, the discharge evolves from Period-one (P1) state to Period-two (P2) state, so 4.2 mm is taken as a typical to investigate the formation mechanism of P2 discharge. A more detailed study on the effects of gap width will be presented later in this paper.

Figure 2 shows the temporal evolutions of the current density together with the corresponding trajectories constructed by the current density and gas voltage in phase space with the gap widths of 4.0, 4.2, 4.42, and 4.5 mm. As shown in Figure 2a, when the gap width is 4.0 mm, the discharge current pulse is repeated every voltage period, and a stable P1 discharge is obtained. There is only one loop in phase space in Figure 2b, which demonstrates the P1 discharge in Figure 2a. As the gap width is increased to 4.2 mm, the discharge evolves into a P2 state in Figure 2c and the current period is twice the voltage period. It is clear that two different loops in phase space are obtained in Figure 2d. Then, continuing to increase the gap width, the chaotic discharge is obtained in Figure 2e, corresponding to many different loops in phase space in Figure 2f. The chaos lasts over a small gap width interval, and as the gap width increases to 4.5 mm, a clear Period-three (P3) discharge is presented in Figure 2g, where the current density repeats every three voltage periods. In Figure 2h, three different loops in phase space are presented. In fact, the existence of P3 discharge is often accompanied by chaos according to the Li–Yorke theory [58].

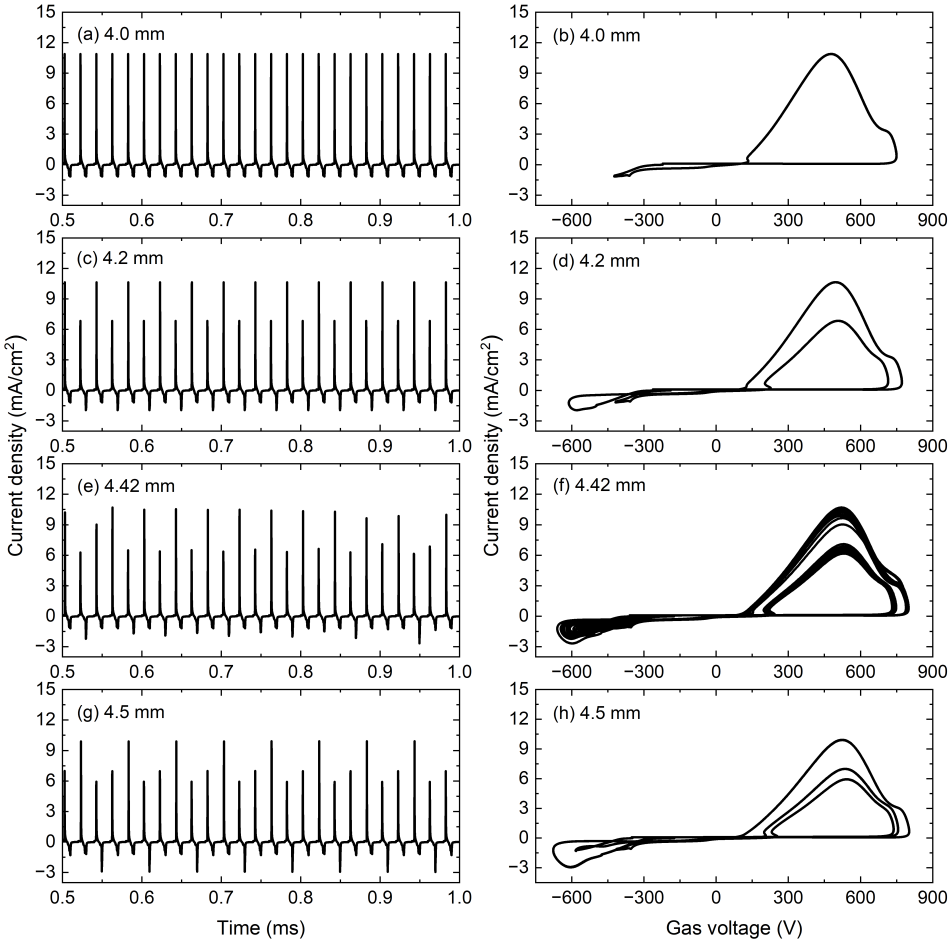

Figure 2. Temporal evolutions of discharge current density with the gap widths of 4.0 mm (**a**), 4.2 mm (**c**), 4.42 mm (**e**), and 4.5 mm (**g**), together with the corresponding trajectories in phase space with the gap widths of 4.0 mm (**b**), 4.2 mm (**d**), 4.42 mm (**f**), and 4.5 mm (**h**).

Then, as the gap width further increases, the discharge evolves into a reverse discharge with a weak positive discharge and a strong negative discharge. The temporal evolutions of the current density and the corresponding trajectories in phase space with the gap widths of 5.0, 5.1, and 5.16 mm are given in Figure 3. As shown in Figure 3a, the discharge enters a reverse chaotic discharge, which is demonstrated in Figure 3b, where the trajectories in phase space are no longer periodic. With the further increasing gap width to 5.1 mm, the Reverse Period-two (RP2) discharge is obtained in Figure 3c. Similar to P2, the repetition period of discharge current doubles the voltage periods. The two larger loops in the third quadrant of Figure 3d clearly show that the discharge maintains a stable RP2 discharge. As shown in Figure 3e, when the gap width is increased to 5.16 mm, the discharge transits into the Reverse Period-one (RP1) discharge through an inverse period-doubling bifurcation, the corresponding trajectory in phase space presents only one loop in Figure 3f.

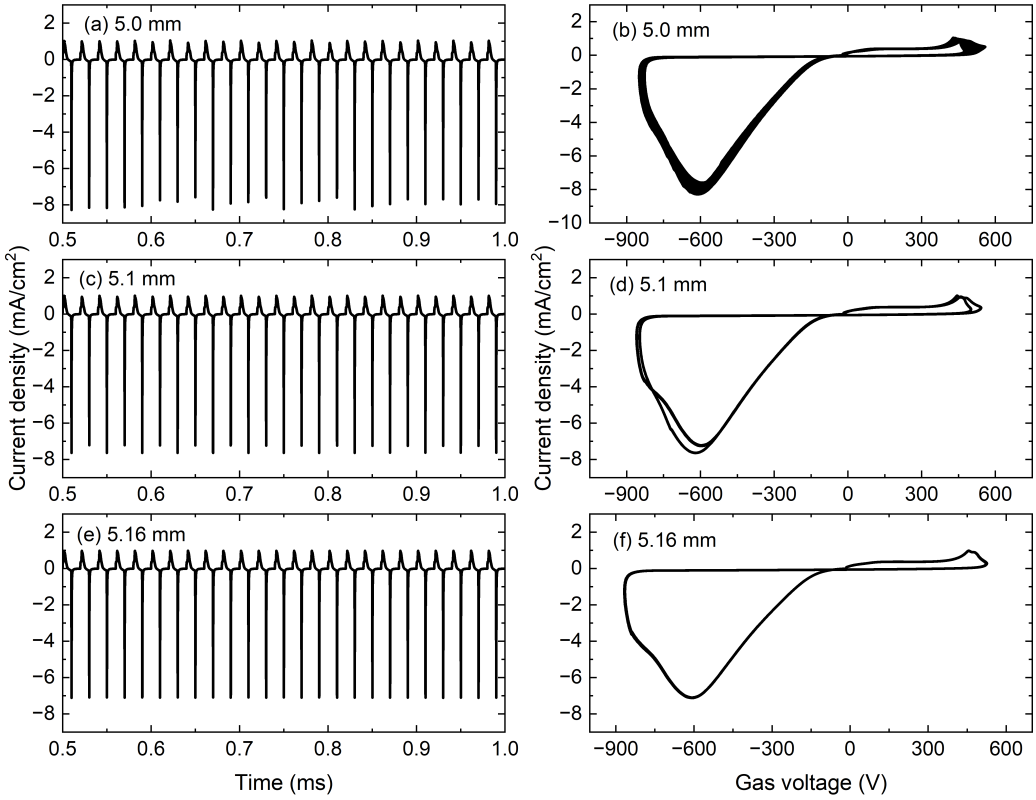

Figure 3. Temporal evolutions of discharge current density with the gap widths of 5.0 mm (**a**), 5.1 mm (**c**), and 5.16 mm (**e**), together with the corresponding trajectories in phase space with the gap widths of 5.0 mm (**b**), 5.1 mm (**d**), and 5.16 mm (**f**).

From the foregoing discussion, there is only a large positive current pulse during the power-on phase and the discharge is a stable P1 state when the width gap is 4.0 mm. Figure 4 plots the temporal evolutions of current density, applied voltage, gas voltage, and memory voltage in P1 discharge with a width gap of 4.0 mm, where the black solid line, green dotted line, red dashed line, and blue dot-dashed line denote the current density, applied voltage, gas voltage, and memory voltage, respectively. During the voltage rise phase, the gas voltage increases with the applied voltage. The CO_2 gas is ignited when the gas voltage reaches 750 V, a lot of charged particles are generated, and a large current pulse with a peak value of 10.9 mA/cm^2 is obtained. At the same time, the charged particles are driven to the surface of the dielectric barriers by the applied electric field, building a reverse induced electric field, which rapidly improves the memory voltage and reduces the gas voltage, resulting in the extinguishing of the discharge. During the voltage fall phase, the reverse electric field could lead to a weak reverse discharge, and the peak current density is only $-1.2\,mA/cm^2$.

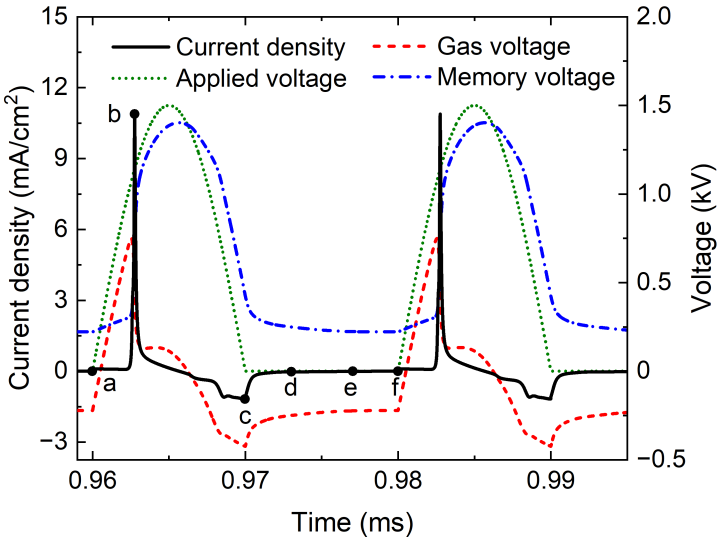

Figure 4. Temporal evolutions of current density, applied voltage, gas voltage, and memory voltage in P1 discharge with a gap width of 4.0 mm.

To investigate the spatiotemporal behavior of the electrons and heavy ions produced by the CO_2 discharge, Figure 5 shows the spatial distributions of positive charge density, negative charge density, electron density, and electric field at several key moments in P1 discharge, and these key moments are marked in Figure 4. The black solid line, red dashed line, and blue dotted line in Figure 5 denote the positive charge density, negative charge density (i.e., the sum of negative ion density and electron density), and electron density, respectively, and the green dot-dashed line represents the electric field in the discharge gap. At the moment a when the applied voltage starts to rise, as shown in Figure 5a, the charged particle density is very low, and the electric field is uniformly distributed throughout the whole discharge gap, with a smaller value of -0.55 kV/cm. This indicates that the charged particles produced by the previous discharge event have completely dissipated. Then, at 2.8 μs after the voltage application, the gas is ignited and the discharge current density rapidly reaches the positive peak value. Figure 5b shows the corresponding spatial distributions of charged particle density and electric field, where the discharge operates in glow mode. In Figure 5b, the cathode fall region, negative glow region, and positive column region could be clearly identified. A strong electric field and large density of positive charges in the cathode fall region are obtained, and the positive column region is quasi-neutrality with almost equal densities of positive and negative charges. In addition, the density of negative charges is almost equal to the density of electrons in Figure 5b, which indicates that electrons are the dominant negative charges in CO_2 discharge under Martian conditions. While in atmospheric CO_2 plasma, the negative charges are mainly composed of CO_3^- ions and electrons [23,24]. At the moment c when the negative current reach the peak value, a wide cathode fall region with a large gradient of positive charge density and a strong electric field is obtained in Figure 5c, and the narrow positive column is characterized by a large plasma density.

When the negative discharge is extinguished, the charged particles in the cathode fall region quickly disappear, while the density of charged particles in the positive column decreases slowly due to the weak electric field and small charged particle density gradient. Therefore, the highest charged particle density can be obtained in the positive column. As shown in Figure 5d, electrons are completely dissipated and the charged particles in the discharge region are mainly heavy ions of CO_2^+ and CO_3^-. The rapid decrease in electron density can be attributed to the following: one is the large transport coefficients of electrons, and the other is the electronegativity of CO_2 gas, which causes many electrons to be attached by CO_2 molecules ($e + CO_2 \rightarrow CO + O^-$). During the power-off phase, the positive and negative ions in the positive column are driven to the electrodes by the

electric field, and the positive column begins to dissipate at about 15 µs after the voltage application. According to the simulation data, a lot of CO_2^+ ions stay in the cathode sheath on the left side of Figure 5d and many CO_3^- ions could be observed in the anode sheath on the right side of Figure 5d. As shown in Figure 5e, although the mobilities of the CO_2^+ and CO_3^- ions are nearly equal, the CO_3^- ions will reach the electrode first because the positive column is closer to the anode. According to the simulation data, when the gap width is 4 mm, the electrons dissipate completely at 12.2 µs, the CO_3^- ions reach the anode at 17.8 µs, and the CO_2^+ ions reach the cathode at 19.5 µs. At the end of the voltage period, the spatial distributions of the charged particles in Figure 5f are the same as those in Figure 5a, which indicates that the ions produced by the discharge are completely dissipated during the power-off phase, without affecting the discharge of the next voltage period.

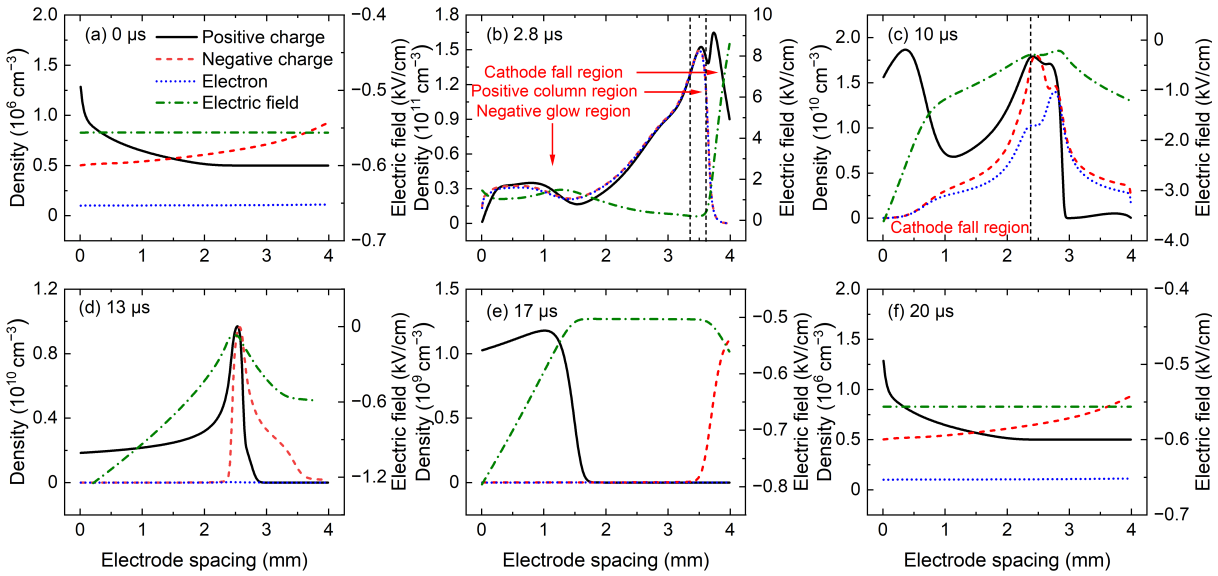

Figure 5. Spatial distributions of positive charge density, negative charge density, electron density, and electric field at several key moments in P1 discharge.

As the gap width increases, the discharge evolves from P1 state into P2 state. Figure 6 shows the current density, applied voltage, gas voltage, and memory voltage in P2 discharge with a gap width of 4.2 mm. In the P2 discharge, the current density is repeated every two voltage periods, and the voltage period in which the largest current pulse is obtained in Figure 6 is regarded as the first voltage period of the P2 discharge. As shown in Figure 6, in the first voltage period, the gas is ignited when the gas voltage reaches 772 V, and a large current pulse with a maximum value of 10.6 mA/cm^2 is observed. However, in the second voltage period, the breakdown voltage is only 715 V, and the corresponding peak current density is only 6.7 mA/cm^2. It is obvious that the breakdown voltage and current density of the second discharge are smaller than those of the first discharge.

To investigate the transformation mechanism from P1 discharge to P2 discharge, Figure 7 gives the spatial distributions of charged particle density and electric field at the moments a–i in P2 discharge, and the moments a–i have been marked in Figure 6. As shown in Figure 7a, at the beginning of the first voltage period, the density of charged particles is very low, and the uniform distributions of the charged particles and electric field are obtained. This means that the heavy ions produced by the previous discharge can reach the surface of dielectric barriers during the power-off phase. Figure 7b shows the spatial distributions of charged particles and electric field at the moment when the positive current reaches the peak value. The discharge operates in glow discharge, the maximum positive charge density in the cathode fall region is 1.6×10^{11} cm^{-3}, and the maximum value of the electric field is 8.5 kV/cm. After the discharge is quenched, the electron density drops rapidly as shown in Figure 7c. According to the simulation results, the electrons are

dissipated at about 13.5 μs with a gap width of 4.2 mm. At 17 μs, there is a positive column with a width of 0.15 mm in the discharge region in Figure 7d, while in the P1 discharge, the positive column at this moment has been completely dissipated. Then, at the end of the first voltage period shown in Figure 7e, the electrons have completely dissipated, but the CO_2^+ and CO_3^- ions cannot reach the electrodes and remain in the sheath region. These ions make the plasma easy to be ignited, reducing the breakdown voltage of the subsequent discharge event.

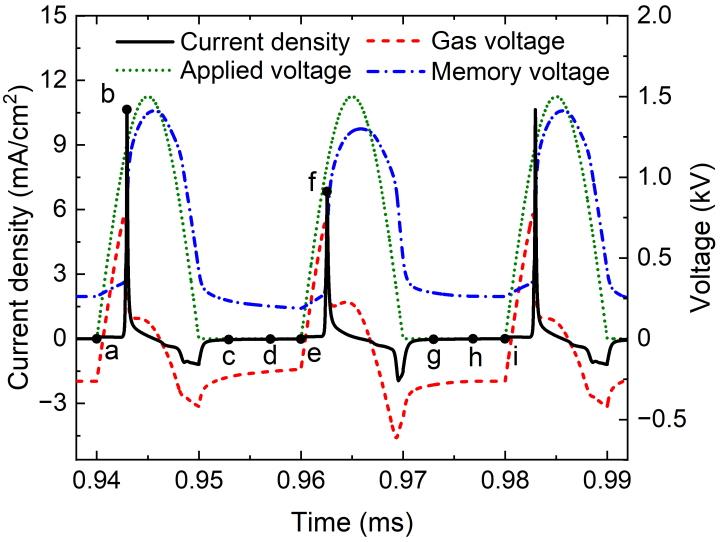

Figure 6. Temporal evolutions of current density, applied voltage, gas voltage, and memory voltage in P2 discharge with a gap width of 4.2 mm.

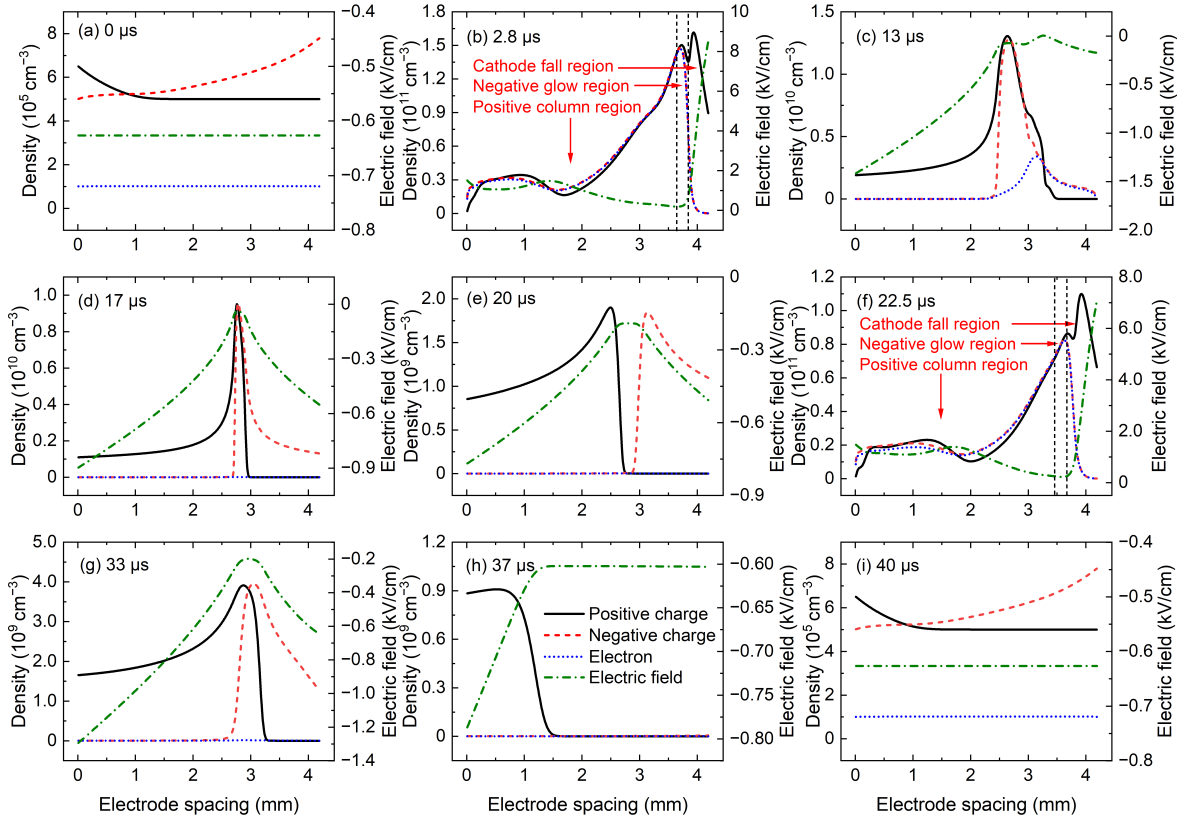

Figure 7. Spatial distributions of positive charge density, negative charge density, electron density, and electric field at several key moments in P2 discharge.

In the second voltage period, the discharge current density reaches the maximum value at 2.5 µs after the voltage application, which is earlier than that in the first voltage period. Figure 7f plots the spatial distributions of charged particle density and electric field at the moment f. Similar to the first discharge, the second discharge also operates in glow mode. The maximum positive charge density in the cathode fall region is only 1.1×10^{11} cm^{-3}, which is obviously smaller than the charged particle density produced by the first discharge event shown in Figure 7b. The second discharge is weak and less charged particles are produced; thus, these charged particles can be completely dissipated during the power-off phase. In fact, the electrons are dissipated completely at about 13 µs in Figure 7g, the heavy CO_3^- ions reach the anode at about 17 µs in Figure 7h, and CO_2^+ ions reach the cathode at about 19 µs according to the simulation results. As shown in Figure 7i, there are no heavy ions remaining in the sheath region at the end of the second voltage period, which does not affect the discharge of the next voltage period. In general, the increase in the gap width prolongs the time for the charged particles to reach the electrodes, so that the heavy ions with small mobility cannot be dissipated during the power-off phase and remain in the sheath region, effectively reducing the breakdown voltage of the next discharge. Then, fewer ions generated by the second discharge event can be completely dissipated during the power-off phase without affecting the third discharge.

When the gap width is increased to 5.1 mm, the discharge turns into a RP2 discharge, a small positive current pulse is followed by a large negative current pulse. Figure 8 shows the temporal evolutions of current density, applied voltage, gas voltage, and memory voltage in PR2 discharge with a gap width of 5.1 mm. It can be seen that, during the voltage rise phase, the rapid increase of the memory voltage suppresses the gas voltage, resulting in a weaker positive discharge. However, during the voltage fall phase, a strong negative discharge caused by the surface charge accumulated on the surface of dielectric barriers can be observed. As shown in Figure 8, the breakdown voltages for the first and second voltage periods are −858 and −846 V, and the corresponding peak current densities are −7.2 and −7.6 mA/cm^2, respectively. In addition, several key moments in RP2 discharge are marked in Figure 8, where a and d are the moments when positive discharge starts (that is, the beginning of the voltage periods) in the first and second voltage periods, b and e are the moments at which the negative discharge begins (i.e., the gas voltage starts to rise in reverse at this moment) in the first and second voltage periods, and c and f are the the moments when the positive current density reaches the maximum values.

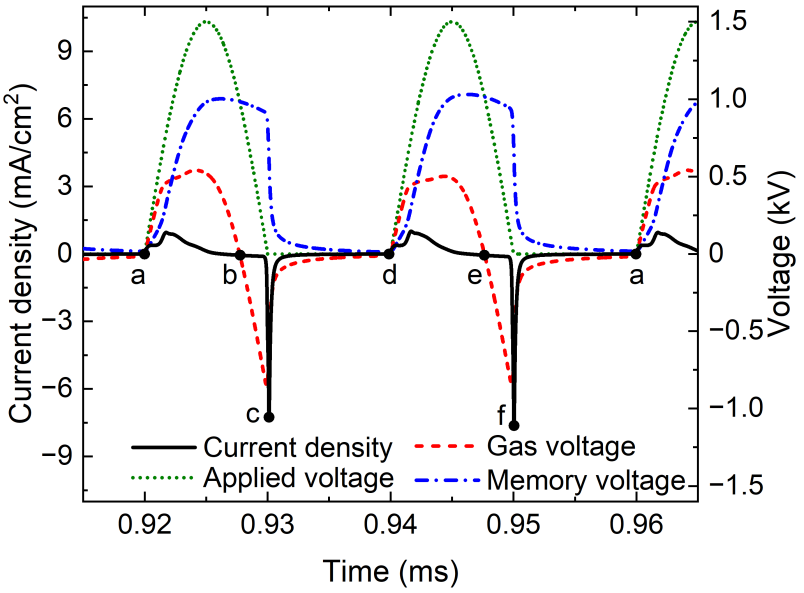

Figure 8. Temporal evolutions of the current density, applied voltage, gas voltage, and memory voltage in PR2 discharge with a gap width of 5.1 mm.

Figure 9 shows the spatial distributions of charged particle density and electric field at the beginning of the positive discharge for two consecutive voltage periods in RP2 discharge. The black and red lines in Figure 9 represent the corresponding spatial distributions at the moments a and d in Figure 8, respectively. As shown in Figure 9, further increasing the gap width allows more charged particles to stay in the discharge gap, and the negative charges are mainly electrons. When the applied voltage begins to rise, these charged particles, especially electrons, are rapidly driven to the surface of the dielectric barriers by the applied electric field to build a reverse electric field, which improves the memory voltage and reduces the gas voltage, resulting in a weak positive discharge and a strong negative discharge.

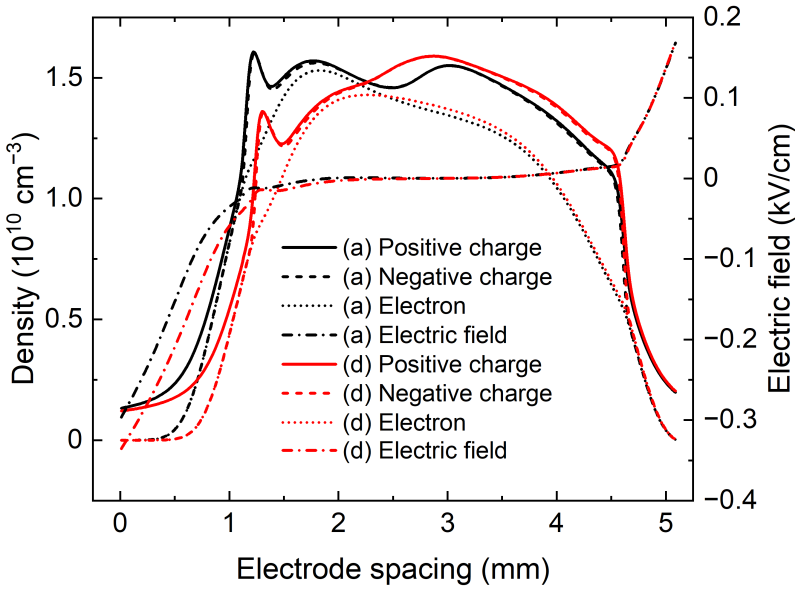

Figure 9. Spatial distributions of positive charge density, negative charge density, electron density, and electric field at the beginning of the positive discharge in RP2 discharge with a gap width of 5.1 mm.

Subsequently, Figure 10 shows the spatial distributions of the charged particle density and electric field at several key moments in the RP2 discharge, where Figure 10a–d plot the corresponding spatial distributions at the moments b, c, e, and f marked in Figure 8, respectively. As shown in Figure 10a, at the moment b, the residual charged particles in the anode sheath and the cathode sheath are CO_3^- and CO_2^+ ions with the maximum densities of 1.1×10^9 and 1.3×10^9 cm^{-3}, respectively. In addition, at the moment e in Figure 10, the densities of residual CO_3^- and CO_2^+ ions in the anode sheath and cathode sheath reach 1.5×10^9 and 1.9×10^9 cm^{-3}, respectively. Obviously, the density of residual ions in the sheath region at the moment e is greater than that at the moment b, thus the discharge of the second voltage period can easily be ignited at a lower voltage. In addition, the discharge current density is determined by the electric field and the charged particle density. According to Figure 10b,d, the higher charged particle density and stronger electric field in the cathode fall region at the moment f in the second voltage period lead to a larger peak current density of the negative discharge.

When the gap width is increased to 5.16 mm, the discharge undergoes an inverse period-doubling bifurcation from RP2 state to RP1 state, and the current density is repeated every voltage period. Figure 11 shows the temporal evolutions of the current density, applied voltage, gas voltage, and memory voltage in RP1 discharge. It is clear that a positive current pulse with a smaller peak value of 0.98 mA/cm^2 can be observed during the voltage rise phase, while a larger positive current pulse is generated during the voltage fall phase; the corresponding breakdown voltage and current density are −865 V and −7.1 mA/cm^2, respectively.

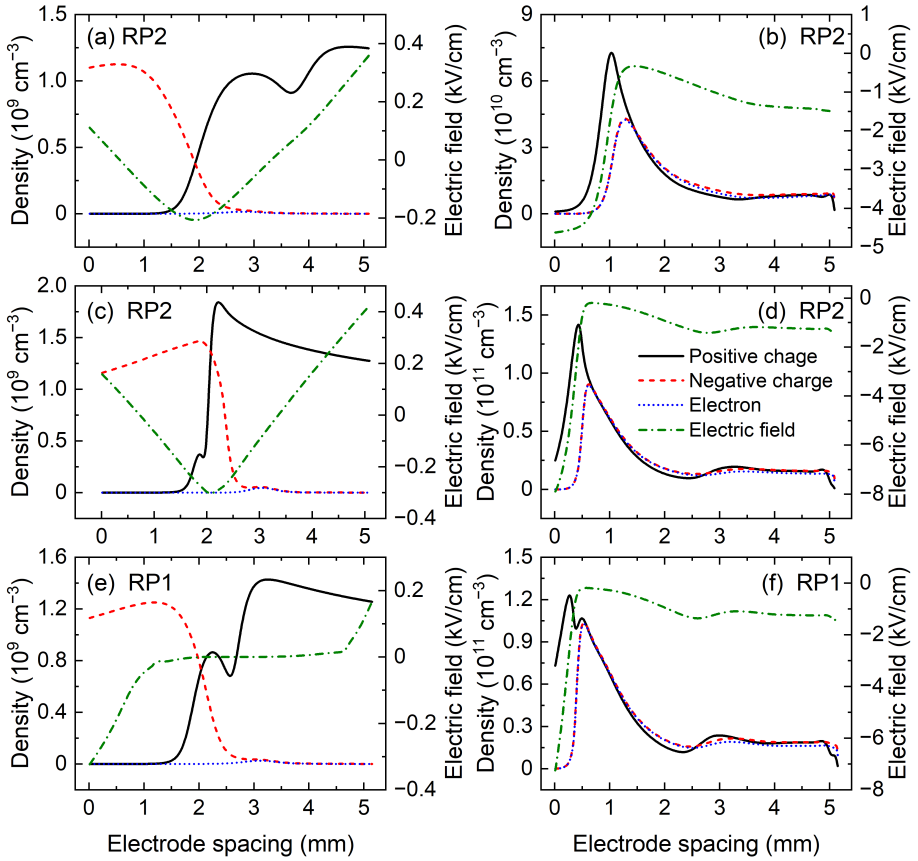

Figure 10. Spatial distributions of positive charge density, negative charge density, electron density, and electric field at several key moments in RP2 discharge and RP1 discharge.

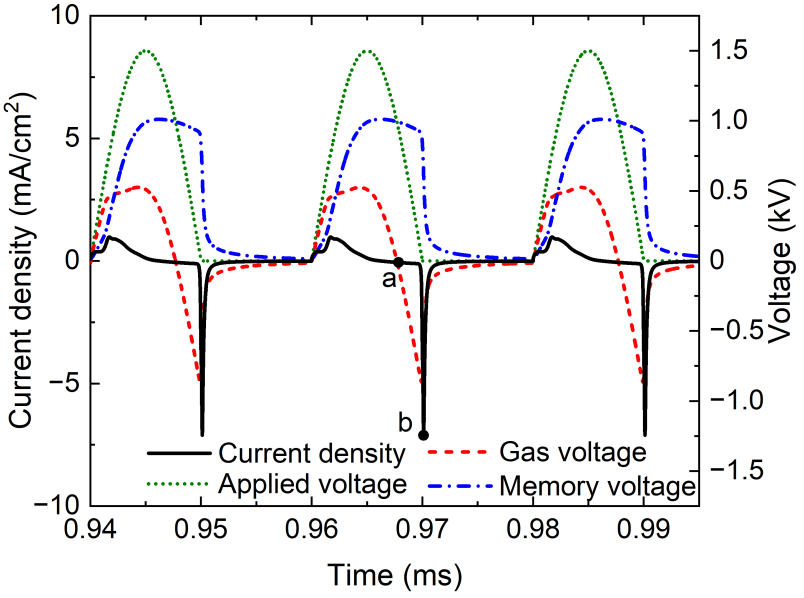

Figure 11. Temporal evolutions of the current density, applied voltage, gas voltage, and memory voltage in RP1 discharge with a gap width of 5.16 mm.

Then, the spatial distributions of positive charge density, negative charge density, electron density, and electric field at the moment a and b in RP1 discharge are given in Figure 10e,f, where the moment a is the moment at which the negative discharge starts, and b is the moment when the negative current density reaches the peak value. In RP1 discharge, at the beginning of each negative discharge, the density and spatial distribution of residual

charged particles are the same. The maximum densities of CO_3^- and CO_2^+ ions staying in the anode sheath and cathode sheath are 1.25×10^9 and 1.43×10^9 cm^{-3}, respectively. In fact, under the same discharge conditions, if the density and spatial distribution of the charged particles staying in the sheath at the beginning of the negative discharge for two consecutive voltage periods are the same, the discharge will be a stable RP1 discharge. As shown in Figure 10f, the reverse discharge in the RP1 state also operates in glow mode.

Figure 12 shows the residual ions density in the sheath region at the beginning of negative discharge for two consecutive voltage periods as a function of gap width in the evolution from RP2 discharge to RP1 discharge. In Figure 12, the black solid line and black dashed line represent the densities of CO_2^+ and CO_3^- ions staying in the sheath region at the beginning of negative discharge in the first voltage period (that is, the moment b in Figure 8), respectively, and the red solid line and the red dashed line represent the densities of CO_2^+ and CO_3^- ions remaining in the sheath region at the beginning of negative discharge in the second voltage period (i.e., the e moment in Figure 8), respectively. As the gap width increases, the densities of residual CO_2^+ and CO_3^- ions in the first voltage period of RP2 discharge increase, while the densities of CO_2^+ and CO_3^- ions in the second voltage period decrease. When the gap width increases to 5.16 mm, the density and spatial distribution of residual ions in the sheath region are completely equal, thus the discharge evolves from RP2 discharge into RP1 discharge. In general, in the RP2 discharge, there are differences in the density and spatial distributions of residual ions in the sheath region at the beginning of the negative discharge for the consecutive voltage periods. As the gap width increases, the density and spatial distribution of the residual ions are gradually equal, resulting in the discharge evolving from RP2 state into RP1 state.

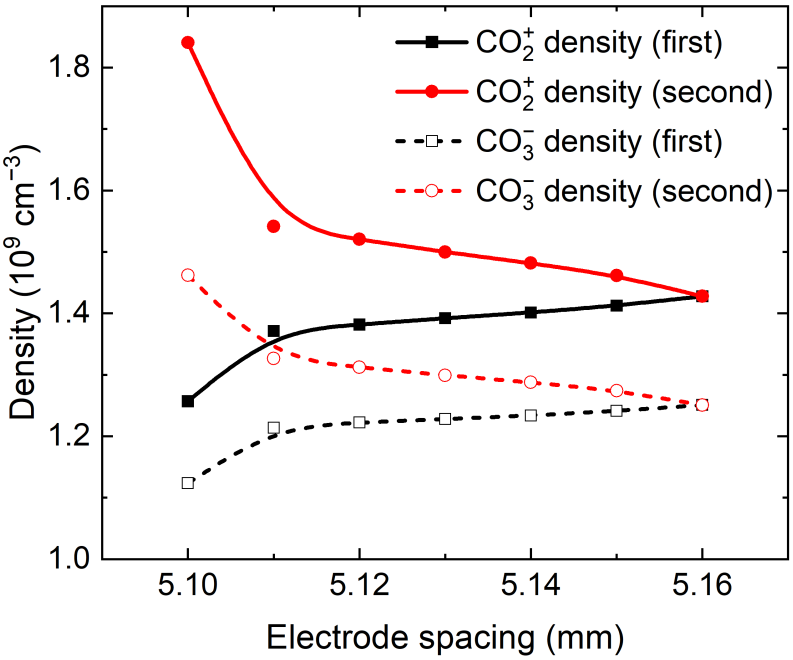

Figure 12. The residual ions density in the sheath region at the beginning of the negative discharge for two consecutive voltage periods as a function of gap width in the evolution from RP2 discharge to RP1 discharge.

It is necessary to investigate the effect of the nonlinear behaviors generated by the increasing gap width on the decomposition of CO_2. In this paper, the discharge power density P_d, Specific Energy Input (SEI), and CO_2 conversion (χ_{CO_2}) are determined by

$$P_d = \frac{1}{Td_g} \int_{t_0}^{t_0+T} I_0 V_g dt \quad (15)$$

$$\mathrm{SEI} = \frac{P_\mathrm{d} t_\mathrm{r}}{e N_{\mathrm{CO_2}}} \tag{16}$$

$$\chi_{\mathrm{CO_2}} = \left(1 - \frac{N_{\mathrm{CO_2}t_\mathrm{r}}}{N_{\mathrm{CO_2}t_0}}\right) \times 100\% \tag{17}$$

where T is the duration of a voltage cycle consisting of the power-on and power-off phases, t_r is the residence time of plasma, $N_{\mathrm{CO_2}t_0}$ and $N_{\mathrm{CO_2}t_\mathrm{r}}$ are the initial CO_2 density and the CO_2 density at the moment t_r, respectively.

According to Figures 2 and 3, an increase in gap width leads to the appearance of temporal nonlinear behaviors in CO_2 discharges and decreases the discharge current density, which reduces the discharge power density P_d. Furthermore, Equation (16) analytically describes that the SEI is mainly determined by power density P_d at a given residence time. Therefore, the growth of gap width can decrease the SEI. In fact, when the gap width increases from 4.0, 4.5 to 5.16 mm at a given residence time of 100 ms, the SEI decreases from 1.63, 1.58, to 1.4 eV/molecule, and CO_2 conversion reduces from 1.49%, 1.22% to 0.75% according to the simulation results.

4. Conclusions

In this study, based on a fluid model, the influence of gap width on temporal nonlinear behaviors in DBDs with CO_2 as the plasma forming gas under Martian pressure is investigated by applying the tailored sinusoidal voltages. The simulation results found that, by increasing the gap width, discharge evolves from P1 discharge into P2 discharge, then converts into chaos, and finally evolves from the RP2 discharge to the RP1 discharge through an inverse period-doubling bifurcation. The simulation data show that, after the CO_2 discharge is extinguished, due to the larger mobility of electrons and the electronegativity of CO_2 gas, a rapid decrease in the electron density is obtained, and the heavy CO_3^- and CO_2^+ ions become the dominant residual charged particles in the discharge gap. In the evolution from P1 discharge to P2 discharge, the increase in the gap width prolongs the time for the CO_3^- and CO_2^+ ions to reach the surface of dielectric barriers, thus these heavy ions cannot be dissipated during the power-off phase and remain in the sheath region, which makes CO_2 gas easy to be ignited at a lower voltage, effectively reducing the breakdown voltage of the next discharge. Then, the second discharge is weaker and fewer charged particles are produced; these charged particles can be completely dissipated during the power-off phase without affecting the third discharge. When the gap width increases to 5.0 mm, more charged particles can stay in the discharge region at the beginning of the voltage period, and the negative charges are mainly electrons. When the applied voltage begins to rise, these residual charged particles are rapidly driven to the surface of the dielectric barriers to build a reverse electric field, which enhances the memory voltage and reduces the gas voltage, resulting in a weak positive discharge and a strong negative discharge. As the gap width continues to increase, the density and spatial distribution of the residual ions in the sheath region for two consecutive voltage periods in the RP2 discharge are gradually equal, resulting in the evolution from RP2 discharge to RP1 discharge. This study contributes to a deeper insight into the effects of gap width on nonlinear behavior in CO_2 DBDs under Martian conditions, and lays the groundwork for optimizing CO_2 discharges.

Author Contributions: Writing—original draft preparation, X.W.; writing—review and editing, X.W., S.G. and Y.Z. All authors have read and agreed to the published version of the manuscript.

Funding: This research was funded by the National Natural Science Foundation of China (No. 11975142).

Institutional Review Board Statement: Not applicable.

Informed Consent Statement: Not applicable.

Data Availability Statement: The data that support the findings of this study are available from the corresponding author upon reasonable request.

Conflicts of Interest: The authors declare no conflict of interest.

References

1. Chen, H.; Du Jonchay, T.S.; Hou, L.; Ho, K. Integrated in situ resource utilization system design and logistics for Mars exploration. *Acta Astronaut.* **2020**, *170*, 80–92. [CrossRef]
2. Zou, Y.; Zhu, Y.; Bai, Y.F.; Wang, L.; Jia, Y.; Shen, W.; Fan, Y.; Liu, Y.; Wang, C.; Zhang, A. Scientific objectives and payloads of Tianwen-1, China's first Mars exploration mission. *Adv. Space Res.* **2021**, *67*, 812–823. [CrossRef]
3. Owen, T.; Biemann, K.; Rushneck, D.R.; Biller, J.E.; Howarth, D.W.; Lafleur, A.L. The composition of the atmosphere at the surface of Mars. *J. Geophys. Res.* **1977**, *82*, 4635–4639. [CrossRef]
4. Guerra, V.; Silva, T.; Ogloblina, P.; Grofulović, M; Terraz, L.; Da Silva, M.L.; Pintassilgo, C.D.; Alves, L.L.; Guaitella, O. The case for in situ resource utilisation for oxygen production on Mars by non-equilibrium plasmas. *Plasma Sources Sci. Technol.* **2017**, *26*, 11LT01. [CrossRef]
5. Hartvigsen, J.J.; Elangovan, S.; Larsen, D.; Elwell, J.; Bokil, M.; Frost, L.J.; Clark, L.M. Challenges of solid oxide electrolysis for production of fuel and oxygen from Mars atmospheric CO_2. *ECS Trans.* **2015**, *68*, 3563. [CrossRef]
6. Landis, G.A.; Linne, D.L. Mars rocket vehicle using in situ propellants. *J. Spacecr. Rocket.* **2001**, *38*, 730–735. [CrossRef]
7. Jiang, Z.; Xiao, T.C.; Kuznetsov, V.L.; Edwards, P.P. Turning carbon dioxide into fuel. *Philos. Trans. R. Soc. A* **2010**, *368*, 3343–3364. [CrossRef]
8. Mei, D.H.; He, Y.L.; Liu, S.Y.; Yan, J.; Tu, X. Optimization of CO_2 conversion in a cylindrical dielectric barrier discharge reactor using design of experiments. *Plasma Process. Polym.* **2016**, *13*, 544–556. [CrossRef]
9. Manning, H.L.K.; Ten Kate, I.L.; Battel, S.J.; Mahaffy, P.R. Electric discharge in the Martian atmosphere, Paschen curves and implications for future missions. *Adv. Space Res.* **2010**, *46*, 1334–1340. [CrossRef]
10. Barth, E.L.; Farrell, W.M.; Rafkin, S.C.R. Electric field generation in Martian dust devils. *Icarus* **2016**, *268*, 253–265. [CrossRef]
11. Guerra, V.; Silva, T.; Guaitella, O. Living on mars: How to produce oxygen and fuel to get home. *Europhys. News* **2018**, *49*, 15–18. [CrossRef]
12. Kozák, T.; Bogaerts, A. Splitting of CO_2 by vibrational excitation in non-equilibrium plasmas: A reaction kinetics model. *Plasma Sources Sci. Technol.* **2014**, *23*, 045004. [CrossRef]
13. Ogloblina, P.; Morillo-Candas, A.S.; Silva, A.F.; Silva, T.; Tejero-del-Caz, A.; Alves, L.L.; Guaitella, O.; Guerra, V. Mars in situ oxygen and propellant production by non-equilibrium plasmas. *Plasma Sources Sci. Technol.* **2021**, *30*, 065005. [CrossRef]
14. Terraz, L.; Silva, T.; Silva, A.F.; Morillo-Candas, A.; Guaitella, O.; Tejero-del-Caz, A.; Alves, L. L.; Guerra, V. Influence of N_2 on the CO_2 vibrational distribution function and dissociation yield in non-equilibrium plasmas. *J. Phys. D* **2019**, *53*, 094002. [CrossRef]
15. Moss, M. S.; Yanallah, K.; Allen, R. W. K.; Pontiga, F. An investigation of CO_2 splitting using nanosecond pulsed corona discharge: Effect of argon addition on CO_2 conversion and energy efficiency. *Plasma Sources Sci. Technol.* **2017**, *26*, 035009. [CrossRef]
16. George, A.; Shen, B.; Craven, M.; Wang, Y.; Kang, D.; Wu, C.; Tu, X. A Review of Non-Thermal Plasma Technology: A novel solution for CO_2 conversion and utilization. *Renew. Sustain. Energy Rev.* **2021**, *135*, 109702. [CrossRef]
17. Bogaerts, A.; Centi, G. Plasma technology for CO_2 conversion: A personal perspective on prospects and gaps. *Front. Energy Res.* **2020**, *8*, 111. [CrossRef]
18. Aerts, R.; Martens, T.; Bogaerts, A. Influence of vibrational states on CO_2 splitting by dielectric barrier discharges. *J. Phys. Chem. C* **2012**, *116*, 23257–23273. [CrossRef]
19. Brehmer, F.; Welzel, S.; van de Sanden, M.C.M.; Engeln, R. CO and byproduct formation during CO_2 reduction in dielectric barrier discharges. *J. Appl. Phys.* **2014**, *116*, 123303. [CrossRef]
20. Mei, D.H.; Tu, X. Conversion of CO_2 in a cylindrical dielectric barrier discharge reactor: Effects of plasma processing parameters and reactor design. *J. CO_2 Util.* **2017**, *19*, 68–78. [CrossRef]
21. Heijkers, S.; Martini, L.M.; Dilecce, G.; Tosi, P.; Bogaerts, A. Nanosecond pulsed discharge for CO_2 conversion: Kinetic modeling to elucidate the chemistry and improve the performance. *J. Phys. Chem. C* **2019**, *123*, 12104–12116. [CrossRef]
22. Martini, L.M.; Lovascio, S.; Dilecce, G.; Tosi, P. Time-resolved CO_2 dissociation in a nanosecond pulsed discharge. *Plasma Chem. Plasma Process.* **2018**, *38*, 707–718. [CrossRef]
23. Wang, X.C.; Bai, J.X.; Zhang, T.H.; Sun, Y.; Zhang, Y.T. Comprehensive study on discharge characteristics in pulsed dielectric barrier discharges with atmospheric He and CO_2. *Phys. Plasma* **2022**, *29*, 083503. [CrossRef]
24. Wang, X.C.; Zhang, T.H.; Sun, Y.; Wu, Z.C.; Zhang, Y.T. Numerical study on discharge characteristics and plasma chemistry in atmospheric CO_2 discharges driven by pulsed voltages. *Phys. Plasma* **2022**, *29*, 023505. [CrossRef]
25. Ozkan, A.; Dufour, T.; Bogaerts, A.; Reniers, F. How do the barrier thickness and dielectric material influence the filamentary mode and CO_2 conversion in a flowing DBD? *Plasma Sources Sci. Technol.* **2016**, *25*, 045016. [CrossRef]
26. Michielsen, I.; Uytdenhouwen, Y.; Pype, J.; Michielsen, B.; Mertens, J.; Reniers, F.; Meynen, V.; Bogaerts, A. CO_2 dissociation in a packed bed DBD reactor: First steps towards a better understanding of plasma catalysis. *Chem. Eng. J.* **2017**, *326*, 477–488. [CrossRef]
27. Ray, D.; Saha, R. DBD plasma assisted CO_2 decomposition: Influence of diluent gases. *Catalysts* **2017**, *7*, 244. [CrossRef]
28. Zhang, Y.H.; Ning, W.J.; Dai, D. Numerical investigation on the transient evolution mechanisms of nonlinear phenomena in a helium dielectric barrier discharge at atmospheric pressure. *IEEE Trans. Plasma Sci.* **2018**, *47*, 179–192. [CrossRef]

29. Zhang, Y.T.; Wang, D.Z.; Kong, M.G. Complex dynamic behaviors of nonequilibrium atmospheric dielectric-barrier discharges. *J. Appl. Phys.* **2006**, *100*, 063304. [CrossRef]
30. Wang, Y.; Zhang, Y.; Wang, D.Z.; Kong, M.G. Period multiplication and chaotic phenomena in atmospheric dielectric-barrier glow discharges. *Appl. Phys. Lett.* **2007**, *90*, 071501. [CrossRef]
31. Wang, Y.H.; Shi, H.; Sun, J.Z.; Wang, D.Z. Period-two discharge characteristics in argon atmospheric dielectric-barrier discharges. *Phys. Plasma* **2009**, *16*, 063507. [CrossRef]
32. Dai, D.; Zhao, X.F.; Wang, Q.M. Inverse period-doubling bifurcation in an atmospheric helium dielectric barrier discharge. *EPL* **2014**, *107*, 15002. [CrossRef]
33. Shi, H.; Wang, Y.H.; Wang, D.Z. Nonlinear behavior in the time domain in argon atmospheric dielectric-barrier discharges. *Phys. Plasma* **2008**, *15*, 122306. [CrossRef]
34. Li, X.T.; Tan, Z.Y.; Wang, X.L.; Liu, Y.D. Evolution of the discharge mode from chaos to an inverse period-doubling bifurcation in an atmospheric-pressure He/N_2 dielectric barrier discharge in increasing nitrogen content. *IEEE Trans. Plasma Sci.* **2022**, *50*, 619–634. [CrossRef]
35. Dai, D.; Hou, H.X.; Hao, Y.P. Influence of gap width on discharge asymmetry in atmospheric pressure glow dielectric barrier discharges. *Appl. Phys. Lett.* **2011**, *98*, 131503.
36. Ha, Y.; Wang, H.J.; Wang, X.F. Modeling of asymmetric pulsed phenomena in dielectric-barrier atmospheric-pressure glow discharges. *Phys. Plasma* **2012**, *19*, 012308. [CrossRef]
37. Zhang, Y.H.; Dai, D.; Ning, W.J.; Li, L.C. Influence of electron backflow on discharge asymmetry in atmospheric helium dielectric barrier discharges. *AIP Adv.* **2018**, *8*, 095327. [CrossRef]
38. Wang, X.C.; Bai, J.X.; Zhang, T.H.; Sun, Y.; Zhang, Y.T. Comprehensive study on plasma chemistry and products in CO_2 pulsed discharges under Martian pressure. *Vacuum* **2022**, *203*, 111200. [CrossRef]
39. Yuan, X.; Raja, L.L. Computational study of capacitively coupled high-pressure glow discharges in helium. *IEEE Trans. Plasma Sci.* **2003**, *31*, 495–503. [CrossRef]
40. He, J.; Hu, J.T.; Liu, D.W.; Zhang, Y.T. Experimental and numerical study on the optimization of pulse-modulated radio-frequency discharges. *Plasma Sources Sci. Technol.* **2013**, *22*, 035008. [CrossRef]
41. Wang, X.C.; Gao, S.H.; Zhang, Y.T. Numerical study on peak current in pulse-modulated radio-frequency discharges with atmospheric helium–oxygen admixtures. *Plasma Sci. Technol* **2022**, *24*, 085401. [CrossRef]
42. Witasse, O.; Nouvel, J.F.; Lebreton, J.P.; Kofman, W. HF radio wave attenuation due to a meteoric layer in the atmosphere of Mars. *Geophys. Res. Lett.* **2001**, *28*, 3039–3042. [CrossRef]
43. Wang, C.; Fu, Q.; Chang, Z.S.; Zhang, G.J. Investigation on the products distribution, reaction pathway, and discharge mechanism of low-pressure CO_2 discharge by employing a 1D simulation model. *Plasma Processes Polym.* **2021**, *18*, e2000228. [CrossRef]
44. Hagelaar, G.J.M.; De Hoog, F.J.; Kroesen, G.M.W. Boundary conditions in fluid models of gas discharges. *Phys. Rev. E* **2000**, *62*, 1452. [CrossRef] [PubMed]
45. Simeni, M.S.; Zheng, Y.; Barnat, E.V.; Bruggeman, P.J. Townsend to glow discharge transition for a nanosecond pulse plasma in helium: Space charge formation and resulting electric field dynamics. *Plasma Sources Sci. Technol.* **2021**, *30*, 055004. [CrossRef]
46. Murakami, T.; Sakai, O. Rescaling the complex network of low-temperature plasma chemistry through graph-theoretical analysis. *Plasma Sources Sci. Technol.* **2020**, *29*, 115018. [CrossRef]
47. Holmes, T.D.; Rothman, R.H.; Zimmerman, W.B. Graph Theory Applied to Plasma Chemical Reaction Engineering. *Plasma Chem. Plasma Process.* **2021**, *41*, 531–557. [CrossRef]
48. Hagelaar, G.J.M.; Pitchford, L.C. Solving the Boltzmann equation to obtain electron transport coefficients and rate coefficients for fluid models. *Plasma Sources Sci. Technol.* **2005**, *14*, 722. [CrossRef]
49. Grofulović, M.; Alves, L.L.; Guerra, V. Electron-neutral scattering cross sections for CO_2: A complete and consistent set and an assessment of dissociation. *J. Phys. D Appl. Phys.* **2016**, *49*, 395207. [CrossRef]
50. Massman, W.J. A review of the molecular diffusivities of H_2O, CO_2, CH_4, CO, O_3, SO_2, NH_3, N_2O, NO, and NO_2 in air, O_2 and N_2 near STP. *Atmos. Environ.* **1998**, *32*, 1111–1127. [CrossRef]
51. Viehland, L.A.; Mason, E.A. Transport properties of gaseous ions over a wide energy range, IV. *At. Data Nucl. Data Tables* **1995**, *60*, 37–95. [CrossRef]
52. Ellis, H.W.; Pai, R.Y.; McDaniel, E.W.; Mason, E.A.; Viehland, L.A. Transport properties of gaseous ions over a wide energy range. *At. Data Nucl. Data Tables* **1976**, *17*, 177–210. [CrossRef]
53. Ponduri, S.; Becker, M.M.; Welzel, S.; van de Sanden, M.C.M.; Loffhagen, D.; Engeln, R. Fluid modelling of CO_2 dissociation in a dielectric barrier discharge. *J. Appl. Phys.* **2016**, *119*, 093301. [CrossRef]
54. Ember, G.; Ferron, J.R.; Wohl, K. Self-Diffusion coefficients of carbon dioxide at 1180–1680 K. *J. Chem. Phys.* **1962**, *37*, 891–897. [CrossRef]
55. Marrero, T.R.; Mason, E.A. Gaseous diffusion coefficients. *J. Phys. Chem. Ref. Data* **1972**, *1*, 3–118. [CrossRef]
56. Cenian, A.; Chernukho, A.; Borodin, V.; Sliwinski, G. Modeling of plasma-chemical reactions in gas mixture of CO_2 lasers I. gas decomposition in pure CO_2 glow discharge. *Contrib. Plasma Phys.* **1994**, *34*, 25–37. [CrossRef]
57. Dunlop, P.J.; Bignell, C.M. Prediction of the temperature dependence of binary diffusion coefficients of gaseous systems from thermal diffusion factors and diffusion coefficients at 300 K. *Int. J. Thermophys.* **1997**, *18*, 939–945. [CrossRef]
58. Li, T.Y.; Yorke, J.A. Period three implies chaos. In *The Theory of Chaotic Attractors*; Springer: New York, NY, USA, 2004; pp. 77–84.